MATERIALS SCIENCE

Ultrastrong and ductile precipitation-hardened alloy via high antiphase boundary energy

Shuai Dai[1], Yunzhu Shi[1]*, Junyang He[2], Jie Hou[1], Fei Zhang[3], Zhenggang Wu[1], Chao Ma[1], Shaofei Liu[4], Alexander Schökel[5], Yan Ma[6], Shaolou Wei[7], Claudio Pistidda[8], Zhifeng Lei[1]*, Zhaoping Lu[9]*

Coherent precipitation-hardened alloys often struggle to achieve both ultrahigh strength and exceptional ductility due to their limited resistance to dislocation motion and vulnerability to glide plane softening. Here, we tackle these challenges by introducing multicomponent precipitates with much increased antiphase boundary (APB) energy. In a model Ni_3Al-type ($L1_2$) precipitation-hardened face-centered cubic (FCC) NiCo-based alloy, we incorporate multiple elements at the Al sublattice sites within the precipitates, reducing antisite defects and enhancing ordering degree. This process yields multicomponent precipitates with an ultrahigh APB energy (~308 ± 14 millijoules per square meter), which notably strengthens the alloy. Moreover, the exceptionally high APB energy transforms the deformation mechanism from dislocation shearing to stacking fault shearing, thereby avoiding glide plane softening. These result in a tensile yield strength of 1616 ± 9 megapascals, an ultimate tensile strength of 2155 ± 22 megapascals, and a uniform elongation of 10.1 ± 0.3% for the alloy.

INTRODUCTION

Precipitation hardening, also known as aging or particle hardening, stands as a key heat treatment technique for enhancing alloy strength since the early 1900s (*1*, *2*). This process entails the formation of hard particles within the host matrix, effectively impeding dislocation motion and consequently strengthening the alloys (*3*–*5*). Because of its straightforward thermomechanical process and strengthening capability, precipitation hardening remains the most compelling method for alloys to achieve high strength (*6*–*13*).

In recent years, precipitation hardening through forming coherent ordered nanoparticles has taken the lead in designing high-performance alloys (*13*–*16*). The minimal lattice misfit between these precipitates and the matrix reduces the nucleation energy barrier, facilitating the formation of a high number density of nanoparticles. This increased particle density effectively enhances alloy strength (*14*, *17*, *18*). Moreover, these precipitates align perfectly with the matrix on the interface plane, forming a continuous crystalline lattice. During loading, these particles typically impede dislocation motion while allowing dislocations to shear through. This dislocation shearing mechanism enhances dislocation mobility and improves deformation compatibility between the precipitates and the alloy matrix, avoiding localized plastic deformation and preserving ductility (*4*, *13*).

However, coherent ordered precipitates, characterized by low misfit strain with the matrix and low penetrability to dislocations, offer limited intrinsic resistance to dislocation motion, thus substantially diminishing their strengthening effect (*19*, *20*). Moreover, repeated dislocation shearing disrupts the ordered crystal structure of coherent precipitates, diminishing successive dislocation shearing resistance and triggering glide plane softening, which induces the formation of planar slip bands (*21*, *22*). Consequently, inadequate dislocation multiplication and storage within the bands, as well as faint dislocation accumulation outside the bands, deprive the corresponding strain hardenability (*23*, *24*). These pivotal limitations pose formidable challenges in achieving both ultrahigh strength and substantial uniform elongation in coherent precipitation-hardened alloys.

Here, we transcend these limitations by introducing multicomponent precipitates with high antiphase boundary (APB) energy. Using a NiCo-based face-centered cubic (FCC) alloy strengthened by coherent Ni_3Al-type ($L1_2$) precipitates as our model system, we incorporate multiple elements into the Al sublattice sites to form multicomponent precipitates with an exceptionally high APB energy of ~308 ± 14 mJ/m^2. Despite having a soft and fully recrystallized FCC matrix, the aged $(NiCo)_{85.95}(NbTaWTi)_7Al_7B_{0.05}$ (in atomic ratios) alloy shows an ultrahigh yield strength of 1616 ± 9 MPa, an unprecedented ultimate tensile strength of 2155 ± 22 MPa, and an exceptional uniform elongation of 10.1 ± 0.3%. This work opens up avenues for advancing precipitation hardening and developing alloys with both high strength and ductility.

RESULTS

Mechanical properties

We conducted tensile tests on three alloys: an annealed NiCo binary alloy and two modified variants, annealed and aged $(NiCo)_{85.95}Ti_7Al_7B_{0.05}$ and $(NiCo)_{85.95}(NbTaWTi)_7Al_7B_{0.05}$ alloys (see Materials and Methods). For simplicity, we refer to these alloys as NiCo-A, T-AA, and NTWT-AA alloys, respectively. Figure 1A shows the engineering stress-strain curves of these three alloys, along with the corresponding true stress-strain and strain-hardening rate curves of the T-AA

[1]College of Materials Science and Engineering, Hunan University, Changsha, 410082, China. [2]State Key Laboratory of Powder Metallurgy, Central South University, Changsha, 410083, China. [3]Institute of High Energy Physics, Chinese Academy of Sciences, Beijing, 100049, China. [4]Institute of Materials Plainification, Liaoning Academy of Materials, Shenyang 110167, China. [5]Deutsches Elektronen-Synchrotron DESY, Notkestr. 85, 22607 Hamburg, Germany. [6]Department of Materials Science and Engineering, Delft University of Technology, Mekelweg 2, 2628 CD, Delft, Netherlands. [7]Department of Microstructure Physics and Alloy Design, Max Planck Institute for Sustainable Materials, 40237 Düsseldorf, Germany. [8]Department of Materials Design, Institute of Hydrogen Technology, Helmholtz-Zentrum hereon GmbH, 21502 Geesthacht, Germany. [9]Beijing Advanced Innovation Center for Materials Genome Engineering, State Key Laboratory for Advanced Metals and Materials, University of Science and Technology Beijing, Beijing, 100083, China.
*Corresponding author. Email: yzshi@hnu.edu.cn (Y.Z.Shi); zflei@hnu.edu.cn (Z.F.Lei.); luzp@ustb.edu.cn (Z.P.Lu)

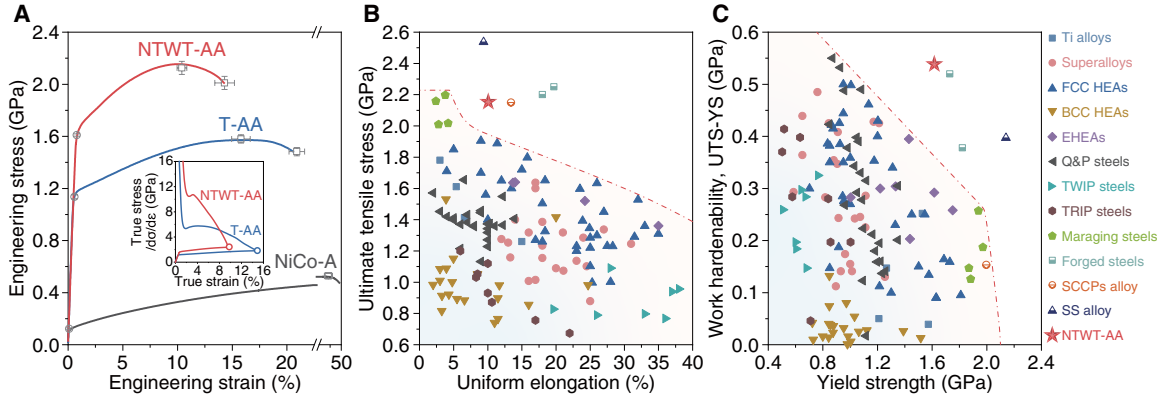

Fig. 1. Mechanical properties. (**A**) Tensile engineering stress-strain curves measured at room temperature for the NiCo-A, T-AA, and NTWT-AA alloys. The inset exhibits the true stress-strain and strain-hardening rate (dσ/dε) curves of the T-AA and NTWT-AA alloys. The NTWT-AA alloy demonstrates ultrahigh strength, large uniform and fracture elongation, and notable strain hardenability. (**B**) Uniform elongation versus ultimate tensile strength, showing the outstanding tensile properties of NTWT-AA alloy, in comparison with titanium (Ti) alloys (*8*), superalloys (*11*, *16*), FCC high-entropy alloys (FCC HEAs) (*17*, *18*, *61*–*65*), body-centered cubic (BCC) HEAs (*24*, *66*, *67*), eutectic high-entropy alloys (EHEAs) (*68*, *69*), quenched and partitioned (Q&P) steels (*70*, *71*), twinning-induced plasticity (TWIP) steels (*72*), transformation-induced plasticity (TRIP) steels (*73*), maraging steels (*14*), forged steels (*74*), alloy containing stepwise controllable coherent nanoprecipitations (SCCPs alloy) (*75*), alloy featuring short-range ordering, and supranano $L1_2$ particle in the FCC matrix (SS alloy) (*76*). (**C**) Yield strength versus work hardenability, defined as the difference between ultimate tensile strength (UTS) and yield strength (YS).

and NTWT-AA alloys (see the inset). The NiCo-A alloy exhibits a very low tensile yield strength of 122 ± 7 MPa and an ultimate tensile strength of 529 ± 21 MPa. The T-AA alloy allows a tensile yield strength of 1135 ± 15 MPa and an ultimate tensile strength of 1572 ± 32 MPa. In contrast, the NTWT-AA alloy has a tensile yield strength of 1616 ± 11 MPa, an ultimate tensile strength of 2155 ± 27 MPa, and a uniform elongation of 10.1 ± 0.3%. It is worth noting that even under ultrahigh strength conditions, the NTWT-AA alloy maintains uniform elongation, seemingly stemming from its exceptional strain-hardening rate (≥2.4 GPa) based on the Considère criterion (the inset in Fig. 1A). The large uniform elongation of our alloy is not attributed to Lüders band deformation, indicating that plastic instability was effectively delayed. The presence of necking and dimples in the fractured NTWT-AA and T-AA alloys validates their ductile features (fig. S1, A to C and G to I). In addition, the NTWT-AA alloy, with its ultrahigh ultimate tensile strength and exceptional fracture elongation, promotes microvoid nucleation and coalescence near the fracture surface (fig. S1, D to F). Figure 1B exhibits the ultimate tensile strength and uniform elongation of NTWT-AA alloy, in comparison to those of other typical alloys. We compared the ultimate tensile strength to highlight the exceptional work hardenability of the alloy we designed, even at ultrahigh yield strength. The NTWT-AA alloy matches the strength of maraging steels while surpassing them with more than double the uniform elongation. Figure 1C compares the tensile yield strength and work hardenability—defined as the difference between ultimate tensile strength and yield strength—of the NTWT-AA alloy with those of representative alloys. The NTWT-AA alloy exhibits both ultrahigh yield strength and exceptional work hardenability. Compared to other alloys with similar yield strength, the present alloy exhibits superior work hardenability (table S1). Furthermore, a comparison of the yield strength and uniform elongation of our alloy with similar fully recrystallized FCC alloys reveals that our design achieved an outstanding combination of these properties (fig. S2). This attainment underscores the effectiveness of introducing multicomponent precipitates to achieve both ultrahigh strength and extraordinary uniform elongation within a soft matrix.

Microstructures

To unravel the strengthening and ductilization mechanisms of the studied alloys, we investigated their microstructures in detail down to the atomic scale. Figure 2A presents synchrotron high-energy x-ray diffraction (XRD) patterns of NiCo-A, T-AA, and NTWT-AA alloys. The NiCo-A alloy exclusively displays a single FCC phase, whereas the other two alloys exhibit dual phases of FCC and $L1_2$. The lattice parameter of FCC phases in the three alloys is 3.532, 3.556, and 3.562 Å, respectively, while that of $L1_2$ precipitates in T-AA and NTWT-AA alloys is 3.585 and 3.596 Å, respectively (fig. S3). Consequently, the lattice misfit between the FCC matrix and $L1_2$ precipitates in T-AA and NTWT-AA alloys amounts to 0.83 and 0.95%, respectively. Figure 2B illustrates the inverse pole figure of the NTWT-AA alloy from the electron backscattered diffraction (EBSD). This alloy comprises fully recrystallized grains with random orientation and an average grain size of 1.7 ± 0.2 μm. Figure 2C presents an enlarged electron channeling contrast image of NTWT-AA alloy, showing a small amount of large primary $L1_2$ precipitates and a host of secondary $L1_2$ precipitates embedded within the matrix. The primary $L1_2$ precipitates form during annealing (at 1050°C for 10 min) and predominantly locate at grain boundaries. The secondary $L1_2$ precipitates develop during aging (at 800°C for 16 hours) and mainly disperse inside grains. The dark-field transmission electron microscopy (TEM) image and the {100} superlattice diffraction spots from selected area electron diffraction patterns further evidence the presence of secondary $L1_2$ precipitates (Fig. 2D). The corresponding average size and spacing along the <110> direction are 36 and 21 nm, respectively (fig. S4, A to C). A representative aberration-corrected scanning transmission electron microscope high-angle annular dark-field (STEM-HAADF) micrograph manifests the fully coherent interface between secondary $L1_2$ precipitates and the FCC matrix (Fig. 2E). In addition, atomic-scale

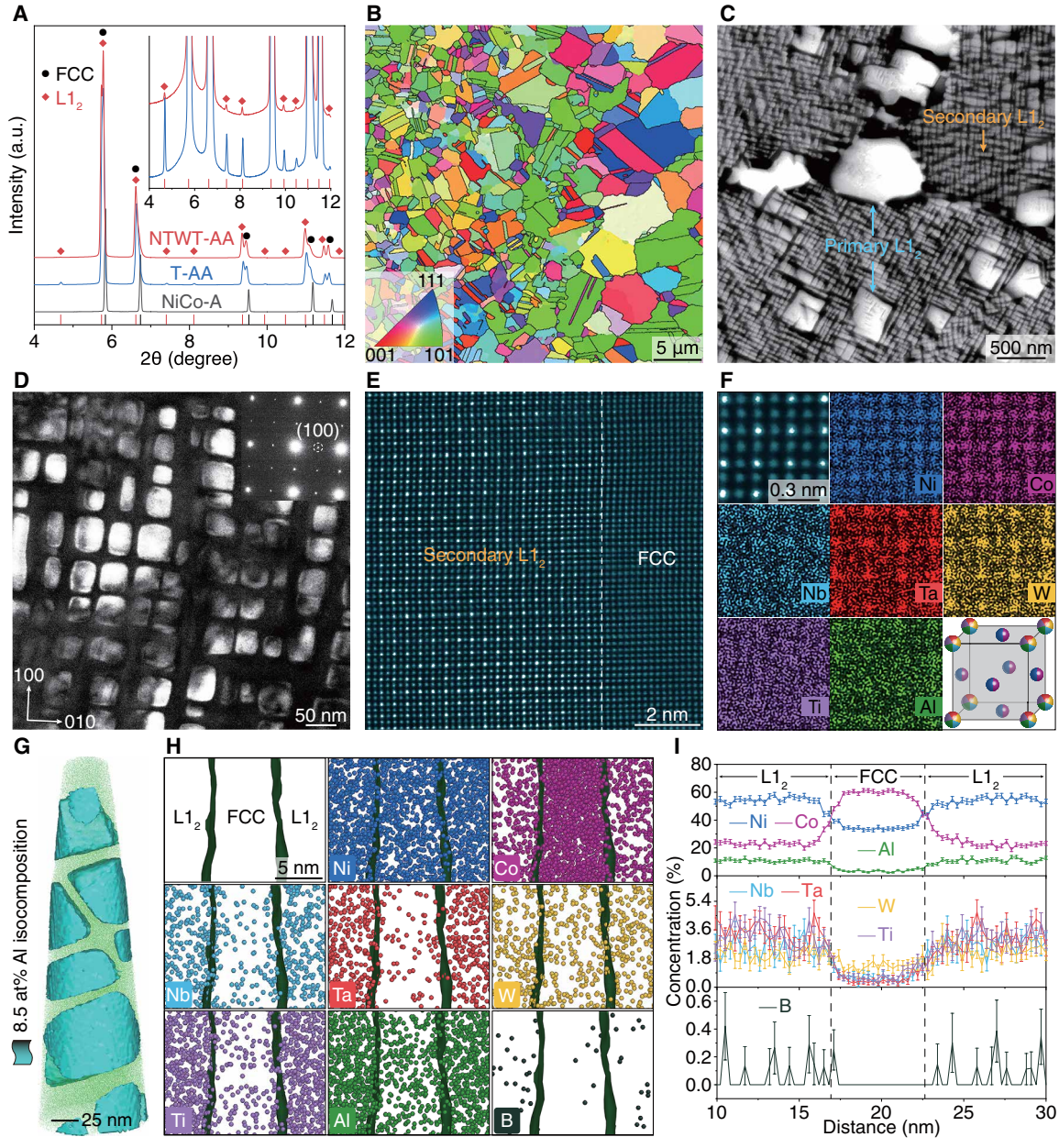

Fig. 2. Microstructures. (**A**) Synchrotron high-energy XRD patterns of the NiCo-A, T-AA, and NTWT-AA alloys, along with an enlarged view of the patterns in the inset. NiCo-A features a single FCC lattice structure, while both T-AA and NTWT-AA alloys adopt a duplex lattice structure comprising FCC and $L1_2$ phases. a.u., arbitrary units. (**B**) EBSD imaging showing a fully recrystallized structure of the NTWT-AA alloys. (**C**) The corresponding electron channeling contrast image revealing large primary $L1_2$ precipitates (indicated by blue arrows) mainly distributed along grain boundaries, alongside small secondary $L1_2$ precipitates (indicated by an orange arrow) primarily located inside grains. (**D**) Dark-field TEM image of secondary $L1_2$ precipitates obtained using the {100} superlattice diffraction spot (see the inset). (**E**) Aberration-corrected STEM-HAADF image confirming the interfacial coherency between the secondary $L1_2$ precipitates and FCC matrix. (**F**) Atomic-scale STEM-HAADF image and the corresponding EDX maps taken from the secondary $L1_2$ precipitate, demonstrating that Ni and Co atoms predominantly occupy the faced centers (Ni sublattice), whereas Nb, Ta, W, Ti, and Al atoms are located at the vertices (Al sublattice). A diagram illustrating the sublattice site occupancy of each element in the $L1_2$ structure is provided for reference. (**G**) APT three-dimensional (3D) reconstruction from the analysis of an NTWT-AA specimen, with the threshold for the iso-composition surface set at 8.5 at % Al, highlighting the presence of secondary $L1_2$ precipitates. (**H** and **I**) Atomic distribution and proximity histograms across the $L1_2$-FCC-$L1_2$ interfaces unveiling the partitioning of Co elements in the FCC matrix, while Ni, Nb, Ta, W, Ti, Al, and B elements in $L1_2$ precipitates.

energy-dispersive x-ray spectroscopy (EDX) mapping demonstrates that Ni and Co atoms predominantly occupy the face centers of the $L1_2$ unit cell (Ni sublattice), while Nb, Ta, W, Ti, and Al atoms are located at the vertices (Al sublattice) (Fig. 2F and fig. S5). Note that the primary $L1_2$ precipitates also exhibit full coherence with the FCC matrix (fig. S6). Further atom probe tomography (APT) measurements of the NTWT-AA alloy are shown in Fig. 2 (G to I). Reconstruction of 8.5 atomic % (at %) Al isocomposition surfaces visualizes cuboidal-shaped secondary $L1_2$ precipitates embedded in the FCC matrix. Atomic distribution and compositional profiles of each element across the $L1_2$-FCC-$L1_2$ interfaces unveil that Ni, Al, Nb, Ta, W, Ti, and B tend to aggregate in the $L1_2$ precipitates, while Co is enriched in the FCC matrix. According to the atomic sublattice site occupancy and chemical composition of the secondary $L1_2$ precipitates in the NTWT-AA alloy (Fig. 2F and table S2), we identify the precipitates as the $(Ni, Co)_3(Nb, Ta, W, Ti, Al)$ phase. Hence, the incorporation of multiple elements at the Al sublattice sites facilitates the formation of these precipitates. Considering the segregation coefficients of Ni, Co, Nb, Ta, W, Ti, and Al elements and applying the lever rule to the phase diagram, the volume fraction of secondary $L1_2$ precipitates is estimated to be 46.4% (section S1 and fig. S7, A to C).

For the T-AA variant, coherent primary and secondary $L1_2$ precipitates also appear in the fully recrystallized matrix, with an average grain size of 2.0 ± 0.3 μm (fig. S8). The average size and spacing of the secondary precipitates along the <110> direction are 30 and 13 nm, respectively (fig. S4, D to F). The corresponding APT measurements indicate that the cuboidal-shaped secondary $L1_2$ precipitates are identified as the $(Ni, Co)_3(Ti, Al)$ phase (table S2 and fig. S7, D and E). The volume fraction of the precipitates is ~54.3% (section S1 and fig. S7, F and G).

Deformation behavior

To clarify how $(Ni, Co)_3(Nb, Ta, W, Ti, Al)$ and $(Ni, Co)_3(Ti, Al)$ precipitates affect the plastic deformation behavior of NTWT-AA and T-AA alloys, respectively, we conducted a detailed analysis of the microstructural evolution during loading. At 0.8% strain in the NTWT-AA alloy, several stacking faults are geometrically confined within the FCC matrix. Occasionally, paired perfect dislocations shear into a secondary $L1_2$ precipitate (left part of Fig. 3A). In addition, as a glissile perfect dislocation cuts into a secondary $L1_2$ precipitate, it immediately dissociates into partial dislocations, initiating the nucleation of superlattice stacking faults within the precipitate (right part of Fig. 3A). By 2% strain, matrix-confined stacking faults persist, but extensive superlattice stacking faults develop in the secondary $L1_2$ precipitates (Fig. 3B). After reaching 4% strain, numerous superlattice stacking faults form in the secondary $L1_2$ precipitates, and the density of stacking faults is also increased in the FCC matrix (Fig. 3C). Aberration-corrected STEM-HAADF images further reveal that the slip of leading partial dislocations with different displacement vectors produces superlattice intrinsic stacking faults in secondary $L1_2$ precipitates and intrinsic stacking faults in the FCC matrix (fig. S9). At the precipitate/matrix interface, the trailing partial dislocations in superlattice stacking faults generate large compressive strains, introducing an incredibly rugged landscape that intensifies the interaction of partial dislocations (Fig. 3E). Unexpectedly, the Lomer-Cottrell locks formed through the reaction of the leading partial dislocations in the FCC matrix and the trailing partial dislocations accommodate plastic flow, serving as a bridge between the two phases (Fig. 3F). The Lomer-Cottrell locks can promote dislocation multiplication and storage in FCC matrix (fig. S10). The successive slip of leading partial dislocations initiates superlattice extrinsic stacking faults in the $L1_2$ precipitates, eventually forming X-shaped stacking fault networks within them (Fig. 3G). The interaction between superlattice stacking faults in the precipitates and stacking faults in the matrix, X-shaped stacking fault within the precipitates, engineer complex stacking fault networks. These networks contribute to the dynamic Hall-Petch effect, thereby reducing the mean free path of dislocations (*25*–*27*). Upon increasing the strain to 8%, the spacing of the stacking faults is refined to 8.7 ± 3.7 nm, intensively restricting dislocation motion (Fig. 3D). Furthermore, the high flow stress ultimately causes superlattice stacking faults to shear into large primary $L1_2$ precipitates (fig. S11). Therefore, the plastic deformation of the NTWT-AA alloy is dominated by a stacking fault shearing mechanism. This stacking fault shearing mechanism occasionally governs high-temperature plastic deformation in NiCo-based and Co-based superalloys but rarely manifests at room temperature (*16*, *28*, *29*).

However, the T-AA variant primarily exhibits plastic deformation dominated by dislocation shearing, which requires paired perfect dislocation shearing (see the inset in Fig. 3I and fig. S12). To further elucidate the differences in deformation behavior between the NTWT-AA and T-AA alloys, we conducted in situ synchrotron high-energy XRD experiments (fig. S13). As shown, the measured superlattice stacking fault probability of $L1_2$ precipitates in the NTWT-AA alloy is much higher than that in the T-AA variant (Fig. 3H and section S2), further demonstrating the stacking fault shearing mechanism in the NTWT-AA alloy. Moreover, we calculated the dislocation density of the two alloys during deformation through in situ synchrotron high-energy XRD measurements and theoretical predictions using the Taylor-type hardening model (Fig. 3I, fig. S14, and section S3) (*30*, *31*). Notably, the experimental dislocation density in the NTWT-AA alloy surpasses that in the T-AA alloy, indicating enhanced dislocation multiplication and storage in the NTWT-AA alloy. Furthermore, the experimental dislocation density in the NTWT-AA alloy is lower than the corresponding theoretical value. This suggests that apart from the strain hardening resulting from dislocation accumulation, the stacking fault shearing mechanism in the NTWT-AA alloy also contributes to obtaining additional strain hardenability.

Multicomponent precipitates with high APB energy

As a glissile perfect dislocation cuts through coherent precipitates from the matrix, it forms an APB. This planar defect reverses the atomic arrangement across the boundary, disrupting the periodic ordering of the crystals and hindering successive perfect dislocation propagation along the same slip trajectory (*19*, *32*, *33*). The APB energy per unit area on the slip plane hence acts as the force per unit length to repel incoming dislocations within the precipitates. The APB energy of ordered intermetallic compounds can notably affect coherent precipitation hardening and the dislocation shear mechanism (*34*, *35*). NTWT-AA and T-AA are both NiCo-based alloys strengthened by Ni_3Al-type precipitates, but they exhibit notable differences in mechanical performance and plastic deformation behavior. To examine these disparities, we estimate the APB energy of the secondary $L1_2$ precipitates in both alloys. Bulk intermetallics were fabricated according to the precise composition of the secondary $L1_2$ precipitates in both alloys (table S2 and fig. S15, A to F). Then, the as-cast ingots were subjected to a prestrain of 3% to introduce superlattice partial dislocation pairs (fig. S15, G to J).

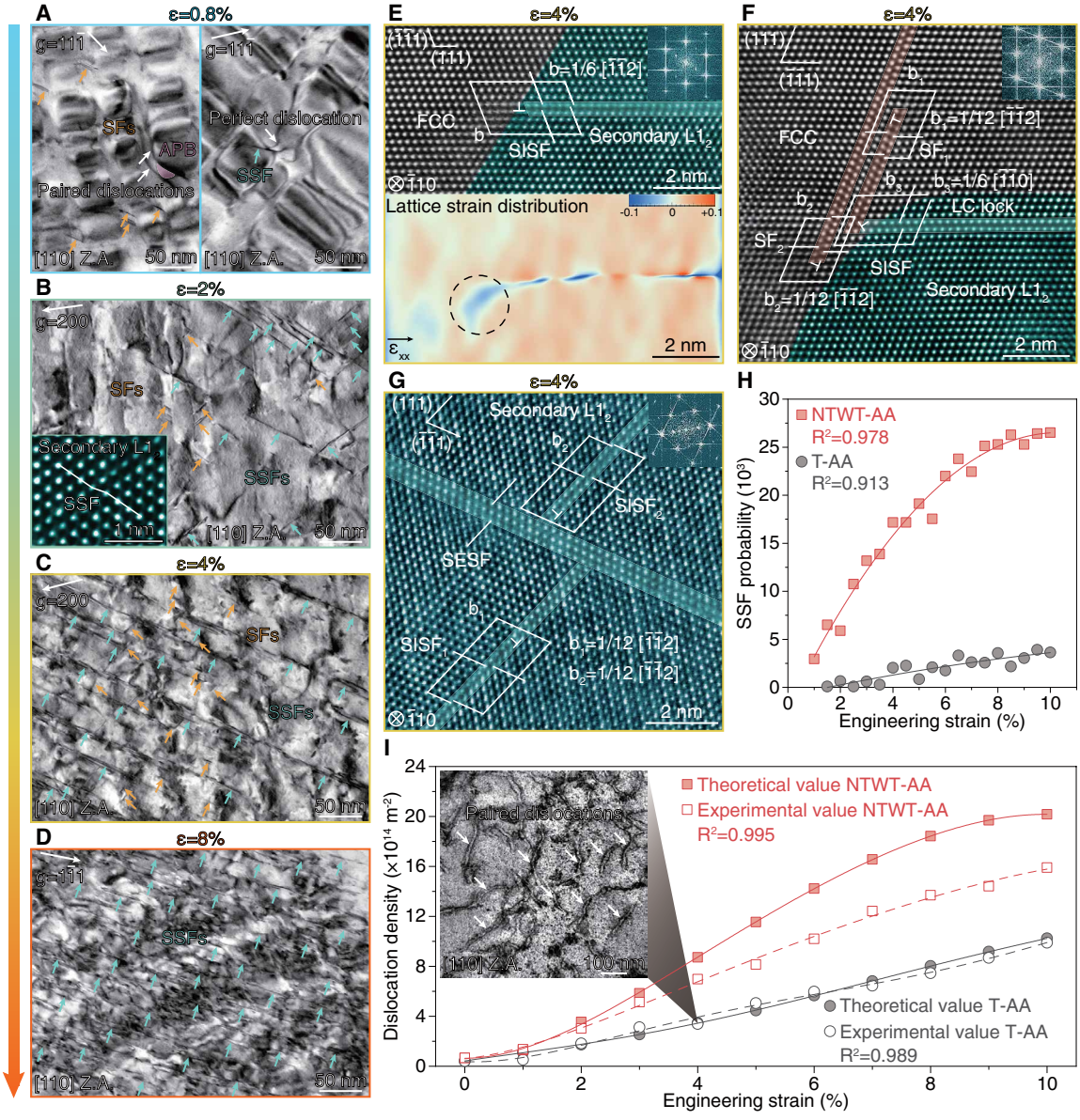

Fig. 3. Deformation mode. (**A** to **D**) Bright-field STEM images of the NTWT-AA alloy strained to 0.8, 2, 4, and 8%. The zone axis (Z.A.) is [110], and *g* represents the operation vector. Orange arrows indicate stacking faults (SFs), green arrows highlight superlattice stacking faults (SSFs), and a purple domain marks an APB. The inserted aberration-corrected STEM-HADDF image in (B) highlights an SSF within a secondary $L1_2$ precipitate. (**E**) STEM-HAADF image (top part) of a superlattice intrinsic stacking fault (SISF) within a secondary $L1_2$ precipitate and the corresponding geometric phase analysis image (bottom part) revealing lattice strain distribution of horizontal normal strain (ε_{xx}). (**F**) STEM-HAADF image showing Lomer-Cottrell (LC) locks formed by the reaction of partial dislocations at the precipitate/matrix interface and in the matrix. (**G**) STEM-HAADF image displaying X-shaped stacking fault networks within secondary $L1_2$ precipitates constructed by superlattice extrinsic stacking faults (SESFs) and SISFs from different slip systems. The fast Fourier transforms of the right insets in (E) to (G) reveal the presence of superlattice diffraction spots corresponding to $L1_2$ precipitates, along with diffuse streaks indicative of SSFs and SFs. (**H**) SSF probability in $L1_2$ precipitates estimated through in situ synchrotron high-energy XRD measurements. (**I**) Engineering strain versus theoretical dislocation density obtained by a Taylor-type hardening model and experimental dislocation density accessed by in situ high-energy XRD measurements. The inset is a representative bright-field STEM image of the T-AA alloy at 4% tensile strain. R^2, coefficient of determination.

Weak-beam dark-field TEM images further reveal numerous perfect superlattice dislocations (Burgers vector $\boldsymbol{b}$ = <110>), which dissociate into superlattice partial dislocation pairs (Burgers vector $\boldsymbol{b}_p$ = 1/2 <110>), separated by the APBs (Fig. 4, A and B, and fig. S16). Superlattice partial dislocation pairs generate strain fields and repulsive interactions that drive their separation, counteracted by the APB surface energy and stacking fault interactions that act to reduce this distance. As APB energy increases, the equilibrium separation of the dislocation pairs decreases. By incorporating the measured separation distance and the inclination angle between the dislocation line and the Burgers vector into anisotropic elasticity theory, we quantitatively determined the APB energy in Ni_3Al-type intermetallics (*36*, *37*). The $(Ni, Co)_3(Nb, Ta, W, Ti, Al)$ intermetallic is expected to have higher APB energy than the $(Ni, Co)_3(Ti, Al)$

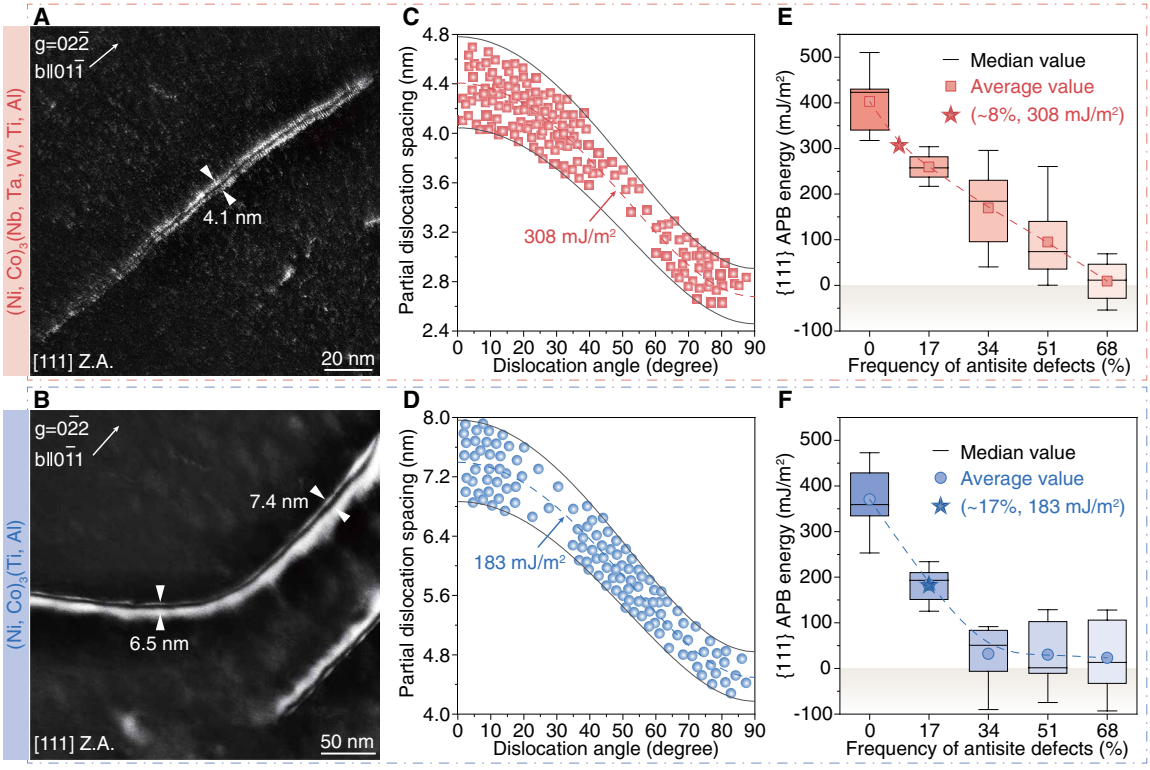

Fig. 4. Multicomponent precipitates with substantially increased APB energy. (**A** and **B**) Weak-beam dark-field TEM images in the 3% strained (Ni, Co)$_3$(Nb, Ta, W, Ti, Al) and (Ni, Co)$_3$(Ti, Al) intermetallics. The zone axis (Z.A.) is [111], and *g* represents the operation vector. (**C** and **D**) The spacing of partial superlattice dislocation pairs as a function of the inclination angle between the dislocation line and its Burgers vector. The calculated APB energy of (Ni, Co)$_3$(Nb, Ta, W, Ti, Al) and (Ni, Co)$_3$(Ti, Al) intermetallics is 308 ± 14 and 183 ± 8 mJ/m^2, respectively. (**E** and **F**) The {111} APB energy versus the frequency of antisite defects in (Ni, Co)$_3$(Nb, Ta, W, Ti, Al) and (Ni, Co)$_3$(Ti, Al) intermetallics. Multi-element incorporation at the Al sublattice sites minimizes antisite defects and improves ordering degree, leading to the formation of multicomponent precipitates with ultrahigh APB energy in the NTWT-AA alloy.

intermetallic due to the shorter separation distance. We then collected the separation distance and the inclination angle between dislocation lines and Burgers vectors, and the corresponding results are plotted in Fig. 4 (C and D). The APB energy of the secondary $L1_2$ precipitates in NTWT-AA and T-AA alloys is then determined to be 308 ± 14 and 183 ± 8 mJ/m^2, respectively (section S4). The APB energy of (Ni, Co)$_3$(Ti, Al) precipitates in the T-AA alloy is consistent with the reported results (*13*, *38*). However, in the NTWT-AA variant, the APB energy of (Ni, Co)$_3$(Nb, Ta, W, Ti, Al) precipitates is about three times higher than that of Ni_3Al precipitates (~110 mJ/m^2) (*39*).

Because of the inevitable presence of antisite defects in ordered intermetallics and their notable impact on ordering degree and APB energy (*40*, *41*), we used density functional theory calculations to investigate the origins of the ultrahigh APB energy of (Ni, Co)$_3$(Nb, Ta, W, Ti, Al) precipitates in the NTWT-AA alloy (section S5 and fig. S17). Figure 4 (E and F) shows the frequency of antisite defects versus the APB energy in (Ni, Co)$_3$(Nb, Ta, W, Ti, Al) and (Ni, Co)$_3$(Ti, Al) precipitates, respectively. Ideally, for a perfectly ordered $L1_2$ precipitate without antisite defects, the APB energy should be close in both precipitates, that is, ~402 ± 71 mJ/m^2 for (Ni, Co)$_3$(Nb, Ta, W, Ti, Al) and ~370 ± 70 mJ/m^2 for (Ni, Co)$_3$(Ti, Al) precipitates. However, with the increase in the frequency of antisite defects, the decreasing trend of APB energy of (Ni, Co)$_3$(Nb, Ta, W, Ti, Al) exhibits a much smoother behavior compared to that of (Ni, Co)$_3$(Ti, Al). When the frequency of antisite defects reaches 34%, the APB energy of (Ni, Co)$_3$(Nb, Ta, W, Ti, Al) decreases to ~170 ± 91 mJ/m^2 while that of (Ni, Co)$_3$(Ti, Al) decreases to ~32 ± 64 mJ/m^2. By combining the experimental APB energies of (Ni, Co)$_3$(Nb, Ta, W, Ti, Al) (308 ± 14 mJ/m^2) and (Ni, Co)$_3$(Ti, Al) (183 ± 8 mJ/m^2), we determined that the frequency of antisite defects in the two precipitates is ~8 and ~17%, respectively. The incorporation of Nb, Ta, W, and Ti into the Al sublattice notably reduces antisite defects, thereby enhancing the ordering degree of Ni_3Al-type intermetallics. To further quantify the difference in ordering degree between (Ni, Co)$_3$(Nb, Ta, W, Ti, Al) and (Ni, Co)$_3$(Ti, Al) intermetallics, we determined their ordering energies. The (Ni, Co)$_3$(Nb, Ta, W, Ti, Al) intermetallic exhibits a lower ordering energy (−0.174 ± 0.004 eV per atom) compared to (Ni, Co)$_3$(Ti, Al) intermetallic (−0.148 ± 0.004 eV per atom), indicating a higher degree of ordering (fig. S18). These findings establish that the suppression of antisite defects and the enhancement of ordering degree underpin the ultrahigh APB energy of multicomponent (Ni, Co)$_3$(Nb, Ta, W, Ti, Al) intermetallic. Different from single-element substitution or mixed substitution of Ni and Al sublattice sites (*13*, *42*, *43*), our approach of incorporating multiple elements (Nb, Ta, W, and Ti) exclusively at the Al sublattice notably enhances the APB energy of the precipitates.

DISCUSSION

We introduced Ni_3Al-type multicomponent precipitates with exceptionally high APB energy, achieving ultrahigh tensile strength and large ductility in a soft and fully recrystallized FCC alloy. The average precipitate sizes for the NTWT-AA and T-AA alloys are 36 and 30 nm, respectively, both falling within the regime dominated by order strengthening (sections S6 and S7 and fig. S19). Thus, we attribute the precipitation hardening in NTWT-AA and T-AA alloys primarily to order strengthening. For the NTWT-AA alloy, the contributions of order strengthening to the total yield strength amount to 1120 MPa, indicating that order strengthening dominates the yield strength. In contrast, for the T-AA variant, the calculated contribution from order strengthening is only 723 MPa, much lower than that of the NTWT-AA alloy (section S6). The theoretically calculated yield strength of the designed alloys closely resembles the experimentally obtained results (fig. S20). Notably, the NTWT-AA alloy exhibits the highest precipitation strengthening effect among all FCC alloys strengthened by coherent Ni_3Al-type precipitates (Fig. 5A). This precipitation strengthening contributes 69.8% to the total theoretical yield strength, supported by its exceptionally high APB energy in multicomponent precipitates (Fig. 5B). Therefore, the increased APB energy enhances order strengthening, thus enhancing the precipitation hardening effect. The ultrahigh critical nucleation stress (~1213 MPa) of dislocations and the unprecedented tensile yield strength (1271 MPa), both resulting from the extremely large APB energy of multicomponent precipitates in NTWT-AA alloy, further confirms this point (sections S8 and S9 and fig. S21).

In the present $L1_2$ precipitation–strengthened NiCo-based alloys, the transition from $(Ni, Co)_3(Ti, Al)$ precipitates with low APB energy to multicomponent $(Ni, Co)_3(Nb, Ta, W, Ti, Al)$ precipitates with high APB energy alters the deformation mode from dislocation

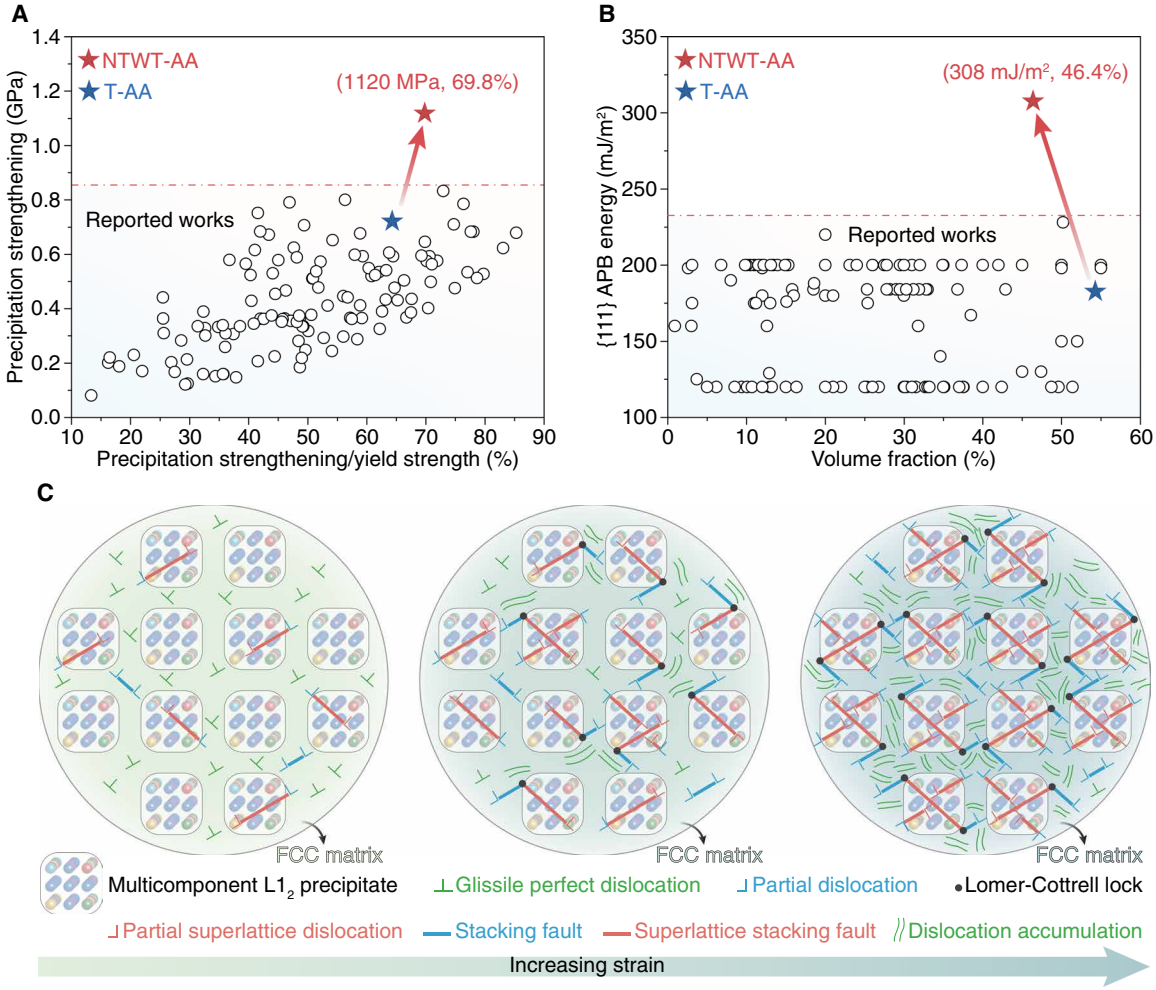

Fig. 5. Origins of ultrahigh tensile yield strength and large ductility. (**A**) Ratio of precipitation strengthening to theoretical yield strength versus precipitation strengthening. The NTWT-AA alloy stands out compared with the T-AA and all Ni_3Al-type ($L1_2$) precipitation-hardened FCC alloys. (**B**) Volume fraction versus {111} APB energy for the Ni_3Al-type precipitates. The NTWT-AA alloy exhibits distinct prominence, setting it apart from the T-AA and all $L1_2$-hardened FCC alloys. Detailed data of (A) and (B) are listed in data S1. (**C**) Schematic illustration of the stacking fault shearing mechanism for NTWT-AA alloy. Glissile perfect dislocations from the FCC matrix immediately transform into partial dislocations upon shearing into the multicomponent precipitates with high APB energy. The partial dislocations eventually shear into the multicomponent precipitates, initiating the stacking fault shearing mechanism. Mutual interaction of partial dislocations promotes nucleation of Lomer-Cottrell locks and constructs densely.

shearing to stacking fault shearing. To explore how APB energy affects the plastic deformation behavior, we initially calculated the stacking fault energies for both FCC matrices (section S10 and fig. S22). The corresponding stacking fault energy of the FCC matrix in NTWT-AA and T-AA alloys is 25 ± 4 and 27 ± 3 mJ/m^2, respectively. Then, we estimated the critical stress for perfect dislocations and Shockley partial dislocations in both alloy matrices (section S11 and fig. S23, A and C). The high critical stress for perfect dislocations suggests that stacking faults dominate the plastic deformation in both FCC matrices, coinciding with the experimental results [left part of Fig. 3A and fig. S23 (B and D)]. Therefore, discrepancies in deformation behavior between NTWT-AA and T-AA alloys primarily stem from the differences in APB energies of their secondary $L1_2$ precipitates. Moreover, in both cases, the characteristics of $L1_2$ precipitates, including morphology, sizes, spacing, volume fraction, and lattice misfit, are comparable, underscoring the notable influence of differences in APB energies on deformation behavior.

When the APB energy of Ni_3Al-type precipitates far surpasses their superlattice stacking fault energy, stacking fault shearing dominates the plastic deformation of the alloy. Otherwise, dislocation shearing will occur (*34*, *44*, *45*). We estimated the superlattice stacking fault energy of secondary $L1_2$ precipitates in both NTWT-AA and T-AA alloys to 181 ± 25 and 208 ± 31 mJ/m^2, respectively (fig. S24). For the NTWT-AA alloy, the APB energy of multicomponent precipitates (308 ± 14 mJ/m^2) far exceeds their superlattice stacking fault energy. As glissile perfect dislocations within the FCC matrix intersect with precipitates, the multicomponent precipitates, characterized by their large APB energy, promote the transformation of these perfect dislocations into partial dislocations (Fig. 5C) (*44*, *46*). These leading partial dislocations effectively shear into the multicomponent precipitates, initiating nucleation sites for superlattice stacking faults within the precipitates (right part of Figs. 3A and 5C). In contrast, for the T-AA variant, the APB energy of the secondary $L1_2$ precipitates (183 ± 8 mJ/m^2) is lower than their superlattice stacking fault energy. As a result, these $L1_2$ precipitates, with diminished APB energy, lower the energy barriers for perfect dislocations to cut through them. Therefore, stacking fault shearing prevails in NTWT-AA alloy, while dislocation shearing predominates in T-AA alloy.

In NTWT-AA alloy, stacking fault shearing retains trailing partial dislocations at precipitate/matrix interfaces, creating an exceptionally rugged landscape that triggers the interaction of partial dislocations (Figs. 3E and 5C). Thus, the Lomer-Cottrell locks generated at precipitate/matrix interfaces, along with superlattice stacking faults in multicomponent precipitates and stacking faults in the matrix, establish stacking fault networks, effectively delocalizing plastic strain between the precipitates and matrix (Figs. 3F and 5C). Also, these Lomer-Cottrell locks can improve dislocation proliferation in the FCC matrix (Figs. 3I and 5C and fig. S10), owing to the sessile and immobile nature of stair-rod dislocations and Frank-Read dislocation sources (*47*–*49*). Meanwhile, the immobile Lomer-Cottrell locks act as strong stabilizers for the stacking fault networks (*50*, *51*). Moreover, the enhanced dislocation density originating from the Lomer-Cottrell locks increases flow stress, prompting more leading partial dislocations from other slip systems to shear into multicomponent precipitates (Fig. 5C). Eventually, the formation of X-shaped stacking fault networks within the multicomponent precipitates effectively prevents leading partial dislocations from cutting through the precipitates (Figs. 3G and 5C). In particular, the reduction of the dislocation mean free path from the X-shaped networks causes a dynamic Hall-Petch effect that contributes to the self-hardening feature of the multicomponent precipitates. Consequently, the multicomponent precipitates effectively mitigate the glide plane softening induced by conventional dislocation shearing, thereby facilitating deformation delocalization, promoting dislocation proliferation, enhancing the dynamic Hall-Petch effect, and eventually contributing to strain hardening.

The strain hardening observed in body-centered cubic high-entropy alloys, which is driven by lattice distortion and deformation-induced destruction of local chemical ordering (*24*, *52*), does not apply to the NTWT-AA alloy. This conclusion is supported by several key facts: the minimal lattice distortion following the nucleation or shearing of multicomponent precipitates, the low sensitivity of lattice distortion to strength enhancement in FCC alloys (*53*, *54*), and the ultrahigh APB energy in multicomponent precipitates, which effectively prevents the transformation from chemical order to disorder.

Previous computational studies demonstrated that substituting the Al sublattice in Ni_3Al-type $L1_2$ precipitates with a single refractory element (e.g., Nb, Ta, W, or Ti) enhances their APB energy (*42*). However, the effects of multi-element co-occupation at this sublattice site remain unexplored. Here, we leverage the high-entropy effect to enable targeted multi-element substitution exclusively at the Al sublattice, achieving a marked increase in APB energy beyond previously reported limits. This approach overcomes a central challenge in earlier experimental studies, where APB energies remained below ~300 mJ/m^2 due to the formation of competing phases in the absence of entropy-driven stabilization (*55*, *56*). Unlike strategies involving simultaneous substitutions at both Ni and Al sublattices (*13*, *43*), our design confines compositional complexity to the Al sublattice, thereby greatly increasing APB energy while preserving phase stability.

To sum up, multicomponent precipitates with an ultrahigh APB energy initiate an ongoing self-hardening mode through a unique stacking fault shearing. This behavior establishes persistent and unparalleled strain hardenability under ultrahigh flow stress. Such exceptional strain hardenability endows the NTWT-AA alloy with substantial ductility at ultrahigh strength.

By examining the intrinsic atomic-scale structure of the precipitates, we use multi-element incorporation at the Al sublattice sites to develop multicomponent Ni_3Al-type $L1_2$ precipitates with an ultrahigh APB energy (~308 ± 14 mJ/m^2) in the soft and fully recrystallized FCC NiCo-based alloy. This notably high APB energy yields a tensile yield strength of 1616 ± 9 MPa, an ultimate tensile strength of 2155 ± 22 MPa, and an impressive uniform elongation of 10.1 ± 0.3%. The unprecedented APB energy notably enhances order strengthening, notably contributing to yield strength and also conferring resistance to paired perfect dislocation shearing, transforming dislocation shearing into stacking fault shearing during loading. Thus, the stacking faults within the FCC matrix, combined with dense superlattice stacking faults in the $L1_2$ multicomponent precipitates, cooperatively form Lomer-Cottrell locks and intricate stacking fault networks. This stacking fault–driven deformation mechanism gives rise to exceptional strain hardenability, resulting in ultrahigh ultimate tensile strength and substantial ductility. Our findings provide a viable approach for strengthening while upholding the ductility in precipitation-hardened alloys, thereby expanding its applicability in target scenarios.

MATERIALS AND METHODS

Material preparation

Alloy ingots with nominal compositions of NiCo, $(NiCo)_{85.95}(NbTaWTi)_7Al_7B_{0.05}$, and $(NiCo)_{85.95}Ti_7Al_7B_{0.05}$ (at %) were fabricated by arc-melting a mixture of pure metals and boron (purity, >99.9 wt %) in a Ti-gettered high-purity argon atmosphere. The ingots were remelted at least eight times to ensure chemical homogeneity. Melted alloys were drop-cast into a water-cooled copper mold with dimensions of 10 mm by 10 mm by 70 mm. The samples were homogenized at 1200°C for 2 hours in a high-purity argon atmosphere, followed by water quenching. Then, the homogenized samples were cold-rolled to sheets with a total thickness reduction of 87%. The rolled NiCo, $(NiCo)_{85.95}(NbTaWTi)_7Al_7B_{0.05}$, and $(NiCo)_{85.95}Ti_7Al_7B_{0.05}$ alloys were annealed at 900°, 1050°, and 1050°C for 10 min and then water quenched. Last, the annealed $(NiCo)_{85.95}(NbTaWTi)_7Al_7B_{0.05}$ was aged at 800°C for 16 hours, and the annealed $(NiCo)_{85.95}Ti_7Al_7B_{0.05}$ was aged at 800°C for 4 hours, with both subsequently subjected to water quenching.

Microstructural characterization

Both in situ and ex situ synchrotron high-energy XRD experiments were carried out at the Powder Diffraction and Total Scattering Beamline P02.1 of PETRA III at Deutsches Elektronen-Synchrotron (DESY) in Hamburg, Germany (*57*, *58*). Being operated at 60 keV, the beamline delivered a monochromatic X-ray with a wavelength of ~0.20738 Å. For the in situ experiment, a Kammrath and Weiss stress rig, capable of withstanding loads up to 5 kN, was positioned between the incident beam and a two-dimensional (2D) detector to perform tensile measurements. Subsized tensile specimens with a gauge length of 12 mm and a width of 2 mm were used. The thickness of the sample measured ~0.6 mm. The tensile tests progressed at room temperature with a constant crosshead speed corresponding to an initial strain rate of $\sim 1 \times 10^{-3}$ s^{-1}. The sample-to-detector distance was ~1 m. The beam size of the incident beam was 0.6 mm by 0.6 mm. Calibration procedures were executed using a standard LaB_6 sample to ascertain detector distance and instrument broadening. 2D diffraction patterns were captured every 5 s using a fast area detector Varex XRpad 4343CT (2880 pixels by 2880 pixels) during tensile testing. The integration of 2D Debye-Scherrer diffraction images into 1D diffraction patterns was performed using the GSAS-II software (*59*). To accurately determine the superlattice stacking fault probability, integration along the loading direction was conducted selectively from 87° to 93° (fig. S13). For calculating dislocation density, integration focused on obtaining diffraction patterns of the (331) reflection, specifically from 40° to 50° (figs. S13A and S14). In ex situ experiments, a comprehensive phase constitution was derived by integrating azimuthal angles from 0° to 360°.

EBSD analysis was performed using a Zeiss Gemini 300 microscope equipped with an Oxford Symmetry detector operating at 15 kV, with a step size of 0.04 μm. Microstructure characterization was conducted using a MIRA3 LMU scanning electron microscope (TESCAN Company), operated at 20 kV. The specimens were initially ground with 2000-grit SiC paper, followed by vibratory polishing with a 0.5-μm Al_2O_3 suspension. Last, a second vibratory polishing step was performed using a 0.04-μm SiO_2 suspension.

Microstructure of the NTWT-AA and T-AA samples was characterized by the Field Electron and Ion Company (FEI) Tecnai F20, operated at 200 kV. Talos F200X G2 was used to characterize microstructural evolution at different deformation stages and dislocation substructures. Aberration-corrected STEM (Thermo Fisher Scientific Themis Z in Analytical Instrumentation Center of Hunan University) equipped with a four-quadrant ChemiSTEM Energy Dispersive Spectrometer (EDS) system and operated at an acceleration voltage of 300 kV. The TEM specimens were mechanically polished to a thickness of 50 μm and then twin-jet electropolished using a solution consisting of 10% perchloric acid and 90% ethyl alcohol by volume. The aberration-corrected STEM specimen was prepared by a dual-beam focused ion beam (FIB) system (Helios 5 CX). Initially, a 30-kV voltage was applied for specimen transfer. During the thinning process, the voltage was gradually reduced from 30 to 5 kV. Last, a 2-kV voltage was used for polishing, minimizing damage to the specimen from high-energy Ga ions during thinning.

APT analyses were conducted on the NTWT-AA and T-AA alloys using a Cameca LEAP 5000XR instrument, operated under an ultrahigh vacuum of $\sim 2.5 \times 10^{-11}$ torr. The specimens were maintained at 77 K during measurements, with a target evaporation rate of 3 ions for every 1000 pulses on average, using high-voltage pulsing mode at a 15% pulse fraction. APT specimens were prepared by FIB on a dual-beam FEI Helios 600i. We also used Ga ions with a 2-kV voltage to polish the specimens. The CAMECA integrated visualization and analysis software, IVAS 3.6.14, was used for data processing and 3D atomic reconstruction (*60*).

Mechanical property measurements

A Shimadzu AGS-X-50 kN universal testing machine equipped with a Shimadzu noncontact digital video extensometer was used to conduct room temperature uniaxial tensile tests. The nominal strain rate is 1×10^{-3} s^{-1}. The specimens, cut along the rolling direction from the sheet using electro-discharge machining, comprised two variants of dog-bone specimens. One variant featured a gauge length of 9.58 mm and a cross section of 2.0×1.1 mm^2, and the other boasted a gauge length of 20 mm and a cross section of 5.0×1.1 mm^2. The specimens were mechanically polished with 2000-grit SiC paper. At least five samples of each alloy were tested to ensure the reliability.

Supplementary Materials

The PDF file includes:

Supplementary Text
Figs. S1 to S26
Tables S1 and S2
Legend for data S1
References

Other Supplementary Material for this manuscript includes the following:

Data S1

REFERENCES AND NOTES

1. A. Wilm, *German patent DRP* **244554**, (1906).
2. A. Wilm, Physical metallurgical experiments on aluminum alloys containing magnesium. *Metallurgie* **8**, 223 (1911).
3. P. D. Merica, R. G. Waltenberg, H. Scott, *Heat Treatment of Duralumin* (National Bureau of Standards, 1919).
4. A. J. Ardell, Precipitation hardening. *Metall. Trans. A.* **16**, 2131–2165 (1985).
5. T. Gladman, Precipitation hardening in metals. *Mater. Sci. Technol.* **15**, 30–36 (2013).
6. T. Z. Xin, Y. H. Zhao, R. Mahjoub, J. X. Jiang, A. Yadav, K. Nomoto, R. M. Niu, S. Tang, F. Ji, Z. Quadir, D. Miskovic, J. Daniels, W. Q. Xu, X. Z. Liao, L.-Q. Chen, K. Hagihara, X. Y. Li, S. Ringer, M. Ferry, Ultrahigh specific strength in a magnesium alloy strengthened by spinodal decomposition. *Sci. Adv.* **7**, eabf3039 (2021).

7. W. W. Sun, Y. M. Zhu, R. Marceau, L. Y. Wang, Q. Zhang, X. Gao, C. Hutchinson, Precipitation strengthening of aluminum alloys by room-temperature cyclic plasticity. *Science* **363**, 972–975 (2019).
8. Y. M. Zhu, K. Zhang, Z. C. Meng, K. Zhang, P. Hodgson, N. Birbilis, M. Weyland, H. L. Fraser, S. C. V. Lim, H. Z. Peng, R. Yang, H. Wang, A. J. Huang, Ultrastrong nanotwinned titanium alloys through additive manufacturing. *Nat. Mater.* **21**, 1258–1262 (2022).
9. S. H. Kim, H. Kim, N. J. Kim, Brittle intermetallic compound makes ultrastrong low-density steel with large ductility. *Nature* **518**, 77–79 (2015).
10. G. Liu, G. J. Zhang, F. Jiang, X. D. Ding, Y. J. Sun, J. Sun, E. Ma, Nanostructured high-strength molybdenum alloys with unprecedented tensile ductility. *Nat. Mater.* **12**, 344–350 (2013).
11. C. Joseph, C. Persson, M. Hörnqvist Colliander, Influence of heat treatment on the microstructure and tensile properties of Ni-base superalloy Haynes 282. *Mater. Sci. Eng. A* **679**, 520–530 (2017).
12. Z. F. Lei, X. J. Liu, Y. Wu, H. Wang, S. H. Jiang, S. D. Wang, X. D. Hui, Y. D. Wu, B. Gault, P. Kontis, D. Raabe, L. Gu, Q. H. Zhang, H. W. Chen, H. T. Wang, J. B. Liu, K. An, Q. S. Zeng, T. G. Nieh, Z. P. Lu, Enhanced strength and ductility in a high-entropy alloy via ordered oxygen complexes. *Nature* **563**, 546–550 (2018).
13. T. Yang, Y. L. Zhao, Y. Tong, Z. B. Jiao, J. Wei, J. X. Cai, X. D. Han, D. Chen, A. Hu, J. J. Kai, K. Lu, Y. Liu, C. T. Liu, Multicomponent intermetallic nanoparticles and superb mechanical behaviors of complex alloys. *Science* **362**, 933–937 (2018).
14. S. H. Jiang, H. Wang, Y. Wu, X. J. Liu, H. H. Chen, M. J. Yao, B. Gault, D. Ponge, D. Raabe, A. Hirata, M. W. Chen, Y. D. Wang, Z. P. Lu, Ultrastrong steel via minimal lattice misfit and high-density nanoprecipitation. *Nature* **544**, 460–464 (2017).
15. L. Gu, Y. H. Zhao, Y. Li, R. Hou, F. Liang, R. S. Zhang, Y. X. Wu, Y. Fan, N. N. Liang, B. Zhou, Y. Chen, G. Sha, G. Chen, Y. D. Wang, X. Chen, Ultrastrong and ductile medium-entropy alloys via hierarchical ordering. *Sci. Adv.* **10**, eadn7553 (2024).
16. Z. R. Xiao, J. Y. He, J. Gu, B. Gan, H. Y. Yu, Z. N. Bi, J. H. Du, M. Song, Tensile properties and deformation mechanisms of a new Ni-Co base superalloy from room temperature up to 750 °C. *Intermetallics* **150**, 107697 (2022).
17. Y. J. Liang, L. L. Wang, Y. R. Wen, B. Y. Cheng, Q. L. Wu, T. Q. Cao, Q. Xiao, Y. F. Xue, G. Sha, Y. D. Wang, Y. Ren, X. Y. Li, L. Wang, F. C. Wang, H. N. Cai, High-content ductile coherent nanoprecipitates achieve ultrastrong high-entropy alloys. *Nat. Commun.* **9**, 4063 (2018).
18. B. Gwalani, S. Dasari, A. Sharma, V. Soni, S. Shukla, A. Jagetia, P. Agrawal, R. S. Mishra, R. Banerjee, High density of strong yet deformable intermetallic nanorods leads to an excellent room temperature strength-ductility combination in a high entropy alloy. *Acta Mater.* **219**, 117234 (2021).
19. L. Xiao, D. L. Chen, M. C. Chaturvedi, Shearing of γ″ precipitates and formation of planar slip bands in Inconel 718 during cyclic deformation. *Scr. Mater.* **52**, 603–607 (2005).
20. D. Raabe, B. H. Sun, A. Kwiatkowski Da Silva, B. Gault, H.-W. Yen, K. Sedighiani, P. Thoudden Sukumar, I. R. Souza Filho, S. Katnagallu, E. Jägle, P. Kürnsteiner, N. Kusampudi, L. Stephenson, M. Herbig, C. H. Liebscher, H. Springer, S. Zaefferer, V. Shah, S.-L. Wong, C. Baron, M. Diehl, F. Roters, D. Ponge, Current challenges and opportunities in microstructure-related properties of advanced high-strength steels. *Metall. Mater. Trans. A* **51**, 5517–5586 (2020).
21. A. Melander, Work hardening and softening in a dislocation glide plane with precipitates. *Mater. Sci. Eng.* **34**, 235–240 (1978).
22. V. Gerold, H. P. Karnthaler, On the origin of planar slip in FCC alloys. *Acta Metall.* **37**, 2177–2183 (1989).
23. F. R. N. Nabarro, J. P. Hirth, *Dislocations in Solids* (Elsevier, 2004).
24. L. Wang, J. Ding, S. Chen, K. Jin, Q. Zhang, J. Cui, B. Wang, B. Chen, T. Li, Y. Ren, S. Zheng, K. Ming, W. Lu, J. Hou, G. Sha, J. Liang, L. Wang, Y. Xue, E. Ma, Tailoring planar slip to achieve pure metal-like ductility in body-centred-cubic multi-principal element alloys. *Nat. Mater.* **22**, 950–957 (2023).
25. B. Devincre, T. Hoc, L. Kubin, Dislocation mean free paths and strain hardening of crystals. *Science* **320**, 1745–1748 (2008).
26. F. Otto, A. Dlouhy, C. Somsen, H. Bei, G. Eggeler, E. P. George, The influences of temperature and microstructure on the tensile properties of a CoCrFeMnNi high-entropy alloy. *Acta Mater.* **61**, 5743–5755 (2013).
27. Z. T. Li, S. H. Ma, S. J. Zhao, W. D. Zhang, F. Peng, Q. Li, T. Yang, C. Y. Wu, D. X. Wei, Y. C. Chou, P. K. Liaw, Y. F. Gao, Z. G. Wu, Achieving superb strength in single-phase FCC alloys via maximizing volume misfit. *Mater. Today* **63**, 108–119 (2023).
28. Y. M. Eggeler, J. Müller, M. S. Titus, A. Suzuki, T. M. Pollock, E. Spiecker, Planar defect formation in the γ′ phase during high temperature creep in single crystal CoNi-base superalloys. *Acta Mater.* **113**, 335–349 (2016).
29. B. X. Cao, W. W. Xu, C. Y. Yu, S. W. Wu, H. J. Kong, Z. Y. Ding, T. L. Zhang, J. H. Luan, B. Xiao, Z. B. Jiao, Y. Liu, T. Yang, C. T. Liu, $L1_2$-strengthened multicomponent Co-Al-Nb-based alloys with high strength and matrix-confined stacking-fault-mediated plasticity. *Acta Mater.* **229**, 117763 (2022).
30. T. H. Courtney, *Mechanical Behavior of Materials* (Waveland Press, ed. 2, 2005).
31. H. Li, H. X. Zong, S. Z. Li, S. B. Jin, Y. Chen, M. J. Cabral, B. Chen, Q. W. Huang, Y. Chen, Y. Ren, K. Y. Yu, S. Han, X. D. Ding, G. Sha, J. S. Lian, X. Z. Liao, E. Ma, J. Sun, Uniting tensile ductility with ultrahigh strength via composition undulation. *Nature* **604**, 273–279 (2022).
32. C. T. Chou, P. B. Hirsch, M. Mclean, E. Hondros, Anti-phase domain boundary tubes in Ni_3Al. *Nature* **300**, 621–623 (1982).
33. L. S. Feng, D. Lv, R. K. Rhein, J. G. Goiri, M. S. Titus, A. Van der Ven, T. M. Pollock, Y. Wang, Shearing of γ′ particles in Co-base and Co-Ni-base superalloys. *Acta Mater.* **161**, 99–109 (2018).
34. V. Paidar, D. P. Pope, M. Yamaguchi, Structural stability and deformation behavior of $L1_2$ ordered alloys. *Scr. Metall.* **15**, 1029–1031 (1981).
35. B. Xiao, J. Zhang, S. F. Liu, Y. H. Zhou, J. Ju, J.-J. Kai, Y. L. Zhao, X. W. Yang, L. Y. Xu, S. J. Zhao, T. Yang, Ultrahigh intermediate-temperature strength and good tensile plasticity in chemically complex intermetallic alloys via lamellar architectures. *Acta Mater.* **262**, 119459 (2024).
36. D. M. Dimiduk, A. W. Thompson, J. C. Williams, The compositional dependence of antiphase-boundary energies and the mechanism of anomalous flow in Ni_3Al alloys. *Philos. Mag. A* **67**, 675–698 (1993).
37. D. J. Crudden, A. Mottura, N. Warnken, B. Raeisinia, R. C. Reed, Modelling of the influence of alloy composition on flow stress in high-strength nickel-based superalloys. *Acta Mater.* **75**, 356–370 (2014).
38. Y. Yang, T. Y. Chen, L. Z. Tan, J. D. Poplawsky, K. An, Y. L. Wang, G. D. Samolyuk, K. Littrell, A. R. Lupini, A. Borisevich, E. P. George, Bifunctional nanoprecipitates strengthen and ductilize a medium-entropy alloy. *Nature* **595**, 245–249 (2021).
39. J. Douin, P. Veyssière, P. Beauchamp, Dislocation line stability in Ni_3Al. *Philos. Mag. A* **54**, 375–393 (1986).
40. S. Miura, S. Takizawa, T. Suzuki, Y. Mishima, T. Mohri, Effect of tetragonal distortion introduced by anti-site defect configuration on additional hardening in off-stoichiometric Al-rich Ni_3Al alloys. *Acta Mater.* **53**, 5175–5181 (2005).
41. J. Pelleg, *Diffusion in the Iron Group $L1_2$ and B2 Intermetallic Compounds* (Springer, 2017).
42. E. Z. Chen, A. Tamm, T. Wang, M. E. Epler, M. Asta, T. Frolov, Modeling antiphase boundary energies of Ni_3Al-based alloys using automated density functional theory and machine learning. *npj Comput. Mater.* **8**, 80 (2022).
43. T. Yang, Y. L. Zhao, W. P. Li, C. Y. Yu, J. H. Luan, D. Y. Lin, L. Fan, Z. B. Jiao, W. H. Liu, X. J. Liu, J. J. Kai, J. C. Huang, C. T. Liu, Ultrahigh-strength and ductile superlattice alloys with nanoscale disordered interfaces. *Science* **369**, 427–432 (2020).
44. B. H. Kear, J. M. Oblak, A. F. Giamei, Stacking faults in gamma prime $Ni_3(Al, Ti)$ precipitation hardened nickel-base alloys. *Metall. Trans.* **1**, 2477–2486 (1970).
45. L. Kovarik, R. R. Unocic, J. Li, P. Sarosi, C. Shen, Y. Wang, M. J. Mills, Microtwinning and other shearing mechanisms at intermediate temperatures in Ni-based superalloys. *Prog. Mater. Sci.* **54**, 839–873 (2009).
46. C. M. F. Rae, R. C. Reed, Primary creep in single crystal superalloys: Origins, mechanisms and effects. *Acta Mater.* **55**, 1067–1081 (2007).
47. W. M. Lomer, A dislocation reaction in the face-centred cubic lattice. *Philos. Mag.* **42**, 1327–1331 (1951).
48. A. H. Cottrell, The formation of immobile dislocations during slip. *Philos. Mag.* **43**, 645–647 (1952).
49. J. P. Hirth, J. Lothe, *Theory of Dislocations* (Krieger Publishing Company, ed. 2, 1992).
50. X. L. Wu, Y. T. Zhu, Y. G. Wei, Q. Wei, Strong strain hardening in nanocrystalline nickel. *Phys. Rev. Lett.* **103**, 205504 (2009).
51. L. Fan, T. Yang, Y. L. Zhao, J. H. Luan, G. Zhou, H. Wang, Z. B. Jiao, C. T. Liu, Ultrahigh strength and ductility in newly developed materials with coherent nanolamellar architectures. *Nat. Commun.* **11**, 6240 (2020).
52. B. Chen, S. Li, J. Ding, X. Ding, J. Sun, E. Ma, Trade-off between local chemical order and lattice distortion in affecting dislocation motion in NbTiZr multi-principal element alloys. *Acta Mater.* **272**, 119910 (2024).
53. R. Labusch, A statistical theory of solid solution hardening. *Phys. Stat. Sol.* **41**, 659–669 (1970).
54. O. N. Senkov, J. M. Scott, S. V. Senkova, D. B. Miracle, C. F. Woodward, Microstructure and room temperature properties of a high-entropy TaNbHfZrTi alloy. *J. Alloy. Compd.* **509**, 6043–6048 (2011).
55. L. Fan, T. Yang, J. H. Luan, Z. B. Jiao, Control of discontinuous and continuous precipitation of γ′-strengthened high-entropy alloys through nanoscale Nb segregation and partitioning. *J. Alloy. Compd.* **832**, 154903 (2020).
56. J. M. Guo, B. C. Zhou, S. Qiu, H. J. Kong, M. C. Niu, J. H. Luan, T. L. Zhang, H. Wu, Z. B. Jiao, Achieving ultrahigh strength and ductility in high-entropy alloys via dual precipitation. *J. Mater. Sci. Technol.* **166**, 67–77 (2023).
57. A.-C. Dippel, H.-P. Liermann, J. T. Delitz, P. Walter, H. Schulte-Schrepping, O. H. Seeck, H. Franz, Beamline P02.1 at PETRA III for high-resolution and high-energy powder diffraction. *J. Synchrotron Rad.* **22**, 675–687 (2015).
58. Y. Ma, B. H. Sun, A. Schökel, W. W. Song, D. Ponge, D. Raabe, W. Bleck, Phase boundary segregation-induced strengthening and discontinuous yielding in ultrafine-grained duplex medium-Mn steels. *Acta Mater.* **200**, 389–403 (2020).

59. J. J. Shen, W. Zhang, J. G. Lopes, Y. T. Pei, Z. Zeng, E. Maawad, N. Schell, A. C. Baptista, R. S. Mishra, J. P. Oliveira, Evolution of microstructure and deformation mechanisms in a metastable $Fe_{42}Mn_{28}Co_{10}Cr_{15}Si_5$ high entropy alloy: A combined in-situ synchrotron x-ray diffraction and EBSD analysis. *Mater. Des.* **238**, 112662 (2024).
60. Y. L. Guo, J. Y. He, Z. M. Li, X. X. Wu, W. J. Lu, C. M. Liu, Solidification segregation-driven microstructural evolution of trace yttrium-alloyed TaMoNbZrTiAl refractory high entropy alloys. *Mater. Charact.* **194**, 112495 (2022).
61. J. Y. He, H. Wang, H. L. Huang, X. D. Xu, M. W. Chen, Y. Wu, X. J. Liu, T. G. Nieh, K. An, Z. P. Lu, A precipitation-hardened high-entropy alloy with outstanding tensile properties. *Acta Mater.* **102**, 187–196 (2016).
62. H. L. Peng, L. Hu, J. F. Chen, S. M. Huang, L. J. Li, Y. Y. Yi, F. Zhou, W. P. Fang, I. Baker, Microstructures and deformation mechanisms of the medium-entropy alloy $(NiCoCr)_{76}(Ni_6AlTi)_3$. *Mater. Sci. Eng. A* **849**, 143449 (2022).
63. J. L. Man, B. L. Wu, G. S. Duan, L. Zhang, G. Wan, L. Zhang, N. F. Zou, Y. D. Liu, The synergistic addition of Al, Ti, Mo and W to strengthen the equimolar CoCrFeNi high-entropy alloy via thermal-mechanical processing. *J. Alloy. Compd.* **902**, 163774 (2022).
64. J. T. Fan, X. B. Ji, L. M. Fu, J. Wang, S. Ma, Y. L. Sun, M. Wen, A. D. Shan, Achieving exceptional strength-ductility synergy in a complex-concentrated alloy via architected heterogeneous grains and nano-sized precipitates. *Int. J. Plast.* **157**, 103398 (2022).
65. S. Qin, M. X. Yang, P. Jiang, F. P. Yuan, X. L. Wu, Excellent tensile properties induced by heterogeneous grain structure and dual nanoprecipitates in high entropy alloys. *Mater. Charact.* **186**, 111779 (2022).
66. S. L. Wei, S. J. Kim, J. Y. Kang, Y. Zhang, Y. J. Zhang, T. Furuhara, E. S. Park, C. C. Tasan, Natural-mixing guided design of refractory high-entropy alloys with as-cast tensile ductility. *Nat. Mater.* **19**, 1175–1181 (2020).
67. Z. B. An, A. Li, S. C. Mao, T. Yang, L. Y. Zhu, R. Wang, Z. X. Wu, B. Zhang, R. W. Shao, C. Jiang, B. X. Cao, C. J. Shi, Y. Ren, C. Liu, H. B. Long, J. F. Zhang, W. Li, F. He, L. G. Sun, J. B. Zhao, L. Y. Yang, X. Y. Zhou, X. Wei, Y. M. Chen, Z. G. Lu, F. Z. Ren, C. T. Liu, Z. Zhang, X. D. Han, Negative mixing enthalpy solid solutions deliver high strength and ductility. *Nature* **625**, 697–702 (2024).
68. P. J. Shi, W. L. Ren, T. X. Zheng, Z. M. Ren, X. L. Hou, J. C. Peng, P. F. Hu, Y. F. Gao, Y. B. Zhong, P. K. Liaw, Enhanced strength-ductility synergy in ultrafine-grained eutectic high-entropy alloys by inheriting microstructural lamellae. *Nat. Commun.* **10**, 489 (2019).
69. J. Ren, Y. Zhang, D. Zhao, Y. Chen, S. Guan, Y. Liu, L. Liu, S. Peng, F. Kong, J. D. Poplawsky, G. Gao, T. Voisin, K. An, Y. M. Wang, K. Y. Xie, T. Zhu, W. Chen, Strong yet ductile nanolamellar high-entropy alloys by additive manufacturing. *Nature* **608**, 62–68 (2022).
70. E. J. Seo, L. Cho, Y. Estrin, B. C. De Cooman, Microstructure-mechanical properties relationships for quenching and partitioning (Q&P) processed steel. *Acta Mater.* **113**, 124–139 (2016).
71. E. D. Moor, J. G. Speer, D. K. Matlock, J.-H. Kwak, S.-B. Lee, Effect of carbon and manganese on the quenching and partitioning response of CMnSi steels. *ISIJ Int.* **51**, 137–144 (2011).
72. G. Dini, A. Najafizadeh, R. Ueji, S. M. Monir-Vaghefi, Improved tensile properties of partially recrystallized submicron grained TWIP steel. *Mater. Lett.* **64**, 15–18 (2010).
73. M. Zhang, L. Li, R. Y. Fu, D. Krizan, B. C. De Cooman, Continuous cooling transformation diagrams and properties of micro-alloyed TRIP steels. *Mater. Sci. Eng. A* **438-440**, 296–299 (2006).
74. Y. Li, G. Yuan, L. Li, J. Kang, F. Yan, P. Du, D. Raabe, G. Wang, Ductile 2-GPa steels with hierarchical substructure. *Science* **379**, 168–173 (2023).
75. T. Li, T. Liu, S. Zhao, Y. Chen, J. Luan, Z. Jiao, R. O. Ritchie, L. Dai, Ultra-strong tungsten refractory high-entropy alloy via stepwise controllable coherent nanoprecipitations. *Nat. Commun.* **14**, 3006 (2023).
76. Y.-Q. Yan, W.-H. Cha, S. Liu, Y. Ma, J.-H. Luan, Z. Rao, C. Liu, Z.-W. Shan, J. Lu, G. Wu, Ductilization of 2.6-GPa alloys via short-range ordered interfaces and supranano precipitates. *Science* **387**, 401–406 (2025).
77. J. B. Chen, J. Y. Chen, Q. J. Wang, Y. D. Wu, Q. Li, C. B. Xiao, S. L. Li, Y. D. Wang, X. D. Hui, Enhanced creep resistance induced by minor Ti additions to a second generation nickel-based single crystal superalloy. *Acta Mater.* **232**, 117938 (2022).
78. B. E. Warren, *X-Ray Diffraction* (Dover Publications, 1990).
79. R. P. Reed, R. E. Schramm, Relationship between stacking-fault energy and x-ray measurements of stacking-fault probability and microstrain. *J. Appl. Phys.* **45**, 4705–4711 (1974).
80. S. L. Wei, C. C. Tasan, Deformation faulting in a metastable CoCrNiW complex concentrated alloy: A case of negative intrinsic stacking fault energy? *Acta Mater.* **200**, 992–1007 (2020).
81. J. S. Jeong, W. Woo, K. H. Oh, S. K. Kwon, Y. M. Koo, In situ neutron diffraction study of the microstructure and tensile deformation behavior in Al-added high manganese austenitic steels. *Acta Mater.* **60**, 2290–2299 (2012).
82. T. Ungár, S. Ott, P. G. Sanders, A. Borbély, J. R. Weertman, Dislocations, grain size and planar faults in nanostructured copper determined by high resolution x-ray diffraction and a new procedure of peak profile analysis. *Acta Mater.* **46**, 3693–3699 (1998).
83. T. Ungár, I. Dragomir, Á. Révész, A. Borbély, The contrast factors of dislocations in cubic crystals: The dislocation model of strain anisotropy in practice. *J. Appl. Cryst.* **32**, 992–1002 (1999).
84. G. Ribárik, B. Jóni, T. Ungár, The convolutional multiple whole profile (CMWP) fitting method, a global optimization procedure for microstructure determination. *Crystals* **10**, 623 (2020).
85. R. A. Renzetti, H. R. Z. Sandim, R. E. Bolmaro, P. A. Suzuki, A. Möslang, X-ray evaluation of dislocation density in ODS-Eurofer steel. *Mater. Sci. Eng. A* **534**, 142–146 (2012).
86. J. H. Gao, S. H. Jiang, H. R. Zhang, Y. H. Huang, D. K. Guan, Y. D. Xu, S. K. Guan, L. A. Bendersky, A. V. Davydov, Y. Wu, H. H. Zhu, Y. D. Wang, Z. P. Lu, W. M. Rainforth, Facile route to bulk ultrafine-grain steels for high strength and ductility. *Nature* **590**, 262–267 (2021).
87. S. Qiu, G. P. Zheng, Z. B. Jiao, Alloying effects on phase stability, mechanical properties, and deformation behavior of CoCrNi-based medium-entropy alloys at low temperatures. *Intermetallics* **140**, 107399 (2022).
88. S. S. Sohn, A. Kwiatkowski da Silva, Y. Ikeda, F. Kormann, W. J. Lu, W. S. Choi, B. Gault, D. Ponge, J. Neugebauer, D. Raabe, Ultrastrong medium-entropy single-phase alloys designed via severe lattice distortion. *Adv. Mater.* **31**, e1807142 (2019).
89. M. Schneider, G. Laplanche, Effects of temperature on mechanical properties and deformation mechanisms of the equiatomic CrFeNi medium-entropy alloy. *Acta Mater.* **204**, 116470 (2021).
90. Y. M. Wang, M. W. Chen, F. H. Zhou, E. Ma, High tensile ductility in a nanostructured metal. *Nature* **419**, 912–915 (2002).
91. U. F. Kocks, A statistical theory of flow stress and work-hardening. *Philos. Mag.* **13**, 541–566 (1966).
92. Y. M. Wang, R. T. Ott, A. V. Hamza, M. F. Besser, J. Almer, M. J. Kramer, Achieving large uniform tensile ductility in nanocrystalline metals. *Phys. Rev. Lett.* **105**, 215502 (2010).
93. N. Baluc, R. Schäublin, K. J. Hemker, Methods for determining precise values of antiphase boundary energies in Ni_3Al. *Philos. Mag. Lett.* **64**, 327–334 (1991).
94. P. M. Andersen, J. P. Hirth, J. Lothe, *Theory of Dislocations* (Cambridge Univ. Press, ed. 3rd, 2017).
95. C. L. Fu, Y. Y. Ye, M. H. Yoo, Bulk and defect properties of ordered intermetallics: A first-principles total-energy investigation. *Mat. Res. Soc. Symp. Proc.* **288**, 21–32 (1993).
96. L. M. Hsiung, N. S. Stoloff, Low-energy dislocation structures in cyclically deformed Ni_3Al single crystals. *Acta Metall. Mater.* **42**, 1457–1467 (1994).
97. G. Kresse, J. Hafner, Ab initiomolecular dynamics for open-shell transition metals. *Phys. Rev. B* **48**, 13115–13118 (1993).
98. G. Kresse, J. Hafner, Ab initiomolecular dynamics for liquid metals. *Phys. Rev. B* **47**, 558–561 (1993).
99. P. E. Blöchl, Projector augmented-wave method. *Phys. Rev. B* **50**, 17953–17979 (1994).
100. J. P. Perdew, K. Burke, M. Ernzerhof, Generalized gradient approximation made simple. *Phys. Rev. Lett.* **77**, 3865–3868 (1996).
101. A. V. D. Walle, Multicomponent multisublattice alloys, nonconfigurational entropy and other additions to the Alloy Theoretic Automated Toolkit. *Calphad* **33**, 266–278 (2009).
102. K. V. Vamsi, T. M. Pollock, A new proximate structure for the APB (111) in $L1_2$ compounds. *Scr. Mater.* **182**, 38–42 (2020).
103. N. Kamikawa, K. Sato, G. Miyamoto, M. Murayama, N. Sekido, K. Tsuzaki, T. Furuhara, Stress-strain behavior of ferrite and bainite with nano-precipitation in low carbon steels. *Acta Mater.* **83**, 383–396 (2015).
104. C. A. Schuh, T. G. Nieh, H. Iwasaki, The effect of solid solution W additions on the mechanical properties of nanocrystalline Ni. *Acta Mater.* **51**, 431–443 (2003).
105. E. O. Hall, The deformation and ageing of mild steel: III discussion of results. *Proc. Phys. Soc.* **64**, 747–753 (1951).
106. J. W. Martin, *Precipitation Hardening* (Butterworth-Heinemann, ed. 2nd, 1998).
107. H. Chen, Z. Chen, G. Ji, S. Y. Zhong, H. W. Wang, A. Borbély, Y. B. Ke, Y. Bréchet, Experimental and modelling assessment of ductility in a precipitation hardening AlMgScZr alloy. *Int. J. Plast.* **139**, 102971 (2021).
108. D. N. Seidman, E. A. Marquis, D. C. Dunand, Precipitation strengthening at ambient and elevated temperatures of heat-treatable Al(Sc) alloys. *Acta Mater.* **50**, 4021–4035 (2002).
109. K. E. Knipling, R. A. Karnesky, C. P. Lee, D. C. Dunand, D. N. Seidman, Precipitation evolution in Al-0.1Sc, Al-0.1Zr and Al-0.1Sc-0.1Zr (at.%) alloys during isochronal aging. *Acta Mater.* **58**, 5184–5195 (2010).
110. A. De Luca, D. N. Seidman, D. C. Dunand, Effects of Mo and Mn microadditions on strengthening and over-aging resistance of nanoprecipitation-strengthened Al-Zr-Sc-Er-Si alloys. *Acta Mater.* **165**, 1–14 (2019).
111. J. C. P. Blankenship, E. Hornbogen, J. E. A. Starke, Predicting slip behavior in alloys containing shearable and strong particles. *Mater. Sci. Eng. A* **169**, 33–41 (1993).
112. K. K. Ma, H. M. Wen, T. Hu, T. D. Topping, D. Isheim, D. N. Seidman, E. J. Lavernia, J. M. Schoenung, Mechanical behavior and strengthening mechanisms in ultrafine grain precipitation-strengthened aluminum alloy. *Acta Mater.* **62**, 141–155 (2014).

113. Y. Y. Zhao, H. W. Chen, Z. P. Lu, T. G. Nieh, Thermal stability and coarsening of coherent particles in a precipitation-hardened $(NiCoFeCr)_{94}Ti_2Al_4$ high-entropy alloy. *Acta Mater.* **147**, 184–194 (2018).
114. E. M. Schulson, Y. Xu, P. R. Munroe, S. Guha, I. Baker, The yield strength of off-stoichiometric Ni_3Al with and without boron. *Acta Metall. Mater* **39**, 2971–2975 (1991).
115. S. J. Liang, D. P. Pope, The difference in latent hardening among $L1_2$ ordered alloys. *Metall. Trans. A.* **7**, 887–889 (1976).
116. S. J. Liang, D. P. Pope, The yield stress of $L1_2$ ordered alloys. *Acta Metall.* **25**, 485–493 (1977).
117. M. Tiryakioğlu, J. S. Robinson, M. A. Salazar-Guapuriche, Y. Y. Zhao, P. D. Eason, Hardness-strength relationships in the aluminum alloy 7010. *Mater. Sci. Eng. A* **631**, 196–200 (2015).
118. Q. Q. Ding, Y. Zhang, X. Chen, X. Q. Fu, D. K. Chen, S. J. Chen, L. Gu, F. Wei, H. B. Bei, Y. F. Gao, M. R. Wen, J. X. Li, Z. Zhang, T. Zhu, R. O. Ritchie, Q. Yu, Tuning element distribution, structure and properties by composition in high-entropy alloys. *Nature* **574**, 223–227 (2019).
119. S. F. Liu, W. T. Lin, Y. L. Zhao, D. Chen, G. Yeli, F. He, S. J. Zhao, J. J. Kai, Effect of silicon addition on the microstructures, mechanical properties and helium irradiation resistance of NiCoCr-based medium-entropy alloys. *J. Alloy. Compd.* **844**, 156162 (2020).
120. Z. Wu, H. Bei, G. M. Pharr, E. P. George, Temperature dependence of the mechanical properties of equiatomic solid solution alloys with face-centered cubic crystal structures. *Acta Mater.* **81**, 428–441 (2014).
121. B. D. Wirth, V. V. Bulatov, T. D. D. L. Rubia, Dislocation-stacking fault tetrahedron interactions in Cu. *J. Eng. Mater. Technol.* **124**, 329–334 (2002).
122. K. P. D. Lagerlöf, J. Castaing, P. Pirouz, A. H. Heuer, Nucleation and growth of deformation twins: A perspective based on the double-cross-slip mechanism of deformation twinning. *Philos. Mag. A* **82**, 2841–2854 (2002).
123. M. W. Chen, E. Ma, K. J. Hemker, H. W. Sheng, Y. M. Wang, X. M. Cheng, Deformation twinning in nanocrystalline aluminum. *Science* **300**, 1275–1277 (2003).
124. J. B. Nelson, D. P. Riley, An experimental investigation of extrapolation methods in the derivation of accurate unit-cell dimensions of crystals. *Proc. Phys. Soc.* **57**, 160–177 (1945).
125. J. Zhang, S. H. Ma, Y. X. Xiong, B. Xu, S. J. Zhao, Elemental partitions and deformation mechanisms of $L1_2$-type multicomponent intermetallics. *Acta Mater.* **219**, 117238 (2021).
126. K. Kumar, R. Sankarasubramanian, U. V. Waghmare, Tuning planar fault energies of Ni_3Al with substitutional alloying: First-principles description for guiding rational alloy design. *Scr. Mater.* **142**, 74–78 (2018).
127. Z. Yi, J. Hu, D. D. Wen, Y. H. Deng, Y. Chen, P. Peng, Effects of alloying elements on the super-lattice intrinsic stacking fault energy and ideal shear strength of Ni_3Al crystals. *Comput. Mater. Sci.* **226**, 112203 (2023).
128. K. V. Vamsi, S. Karthikeyan, Deformation modes and yield strength anomaly in $L1_2$ compounds. *J. Alloy. Compd.* **860**, 158411 (2021).
129. Y. F. Wen, J. Sun, J. Huang, First-principles study of stacking fault energies in Ni_3Al intermetallic alloys. *Trans. Nonferrous Met. Soc. Chin.* **22**, 661–664 (2012).
130. A. Breidi, J. Allen, A. Mottura, First-principles modeling of superlattice intrinsic stacking fault energies in Ni_3Al based alloys. *Acta Mater.* **145**, 97–108 (2018).
131. W. C. Yang, P. F. Qu, J. C. Sun, Q. Z. Yue, H. J. Su, J. Zhang, L. Liu, Effect of alloying elements on stacking fault energies of γ and γ′ phases in Ni-based superalloy calculated by first principles. *Vacuum* **181**, 109682 (2020).
132. W. P. Li, T.-H. Chou, T. Yang, W.-S. Chuang, J. C. Huang, J. H. Luan, X. K. Zhang, X. F. Huo, H. J. Kong, Q. F. He, X. H. Du, C.-T. Liu, F.-R. Chen, Design of ultrastrong but ductile medium-entropy alloy with controlled precipitations and heterogeneous grain structures. *Appl. Mater. Today* **23**, 101037 (2021).

Acknowledgments: We acknowledge DESY (Hamburg, Germany), a member of the Helmholtz Association HGF, for the provision of experimental facilities. We thank Z. Liang (Sinomate Institute of Materials Research, Guangzhou, China) for assistance with the weak-beam dark-field TEM experiments. Parts of this research were carried out at PETRA III beamline P02.1, and we would like to thank A. San José Méndez for assistance. Beam time was allocated for proposals I-20230050 and I-20230183. **Funding:** This work was supported by the National Natural Science Foundation of China (nos. 52371153, 52471174, and 52101194), The Fundamental Research Funds for the Central Universities (nos. 531118010621 and 531118010671), and The Science and Technology Innovation Program of Hunan Province (no. 2022RC1083). **Author contributions:** Y.Z.S., Z.F.L., and Z.P.L. supervised and conceived this project. S.D. and Z.W. carried out material fabrication and mechanical and microstructure characterizations. J. He conducted APT characterizations and analyzed the data. S.D., C.M., and S.L. conducted and analyzed TEM experiments. S.D., Y.M., S.W., A.S., F.Z., and C.P. conducted synchrotron XRD experiments and analyzed the data. J.Ho. performed density functional theory calculations and analyzed the data. S.D., Y.Z.S., Z.F.L., and Z.P.L. wrote and revised the manuscript. All authors discussed the results and commented on the manuscript. **Competing interests:** The authors declare that they have no competing interests. **Data and materials availability:** All data needed to evaluate the conclusions in the paper are present in the paper and/or the Supplementary Materials.

Submitted 20 November 2024
Accepted 12 June 2025
Published 18 July 2025
10.1126/sciadv.adu7566